aerospace

MDPI

Article

Thermo-Mechanical Design of the C/C-SiC-Based Thermal Protection Structure for the Forebody of the Hypersonic Sounding Rocket STORT †

Giuseppe Daniele Di Martino [1,*], Thomas Reimer [1], Luis Baier [1], Lucas Dauth [1], Dorian Hargarten [2] and Ali Gülhan [3]

[1] DLR Institute of Structures and Design, Pfaffenwaldring 38-40, 70569 Stuttgart, Germany; thomas.reimer@dlr.de (T.R.); luis.baier@dlr.de (L.B.); lucas.dauth@dlr.de (L.D.)
[2] DLR Space Operations and Astronaut Training, Münchener Straße 20, 82234 Weßling, Germany; dorian.hargarten@dlr.de
[3] DLR Institute of Aerodynamics and Flow Technology, Linder Höhe, 51147 Cologne, Germany; ali.guelhan@dlr.de
* Correspondence: giuseppe.dimartino@dlr.de
† This article is a revised and expanded version of a paper entitled Structure Design of a Sounding Rocket Fairing with a Segmented Filament Winding-Ceramic Matrix Composite Thermal Protection System, which was presented at the 2nd International Conference on High-Speed Vehicle Science Technology, Brugges, Belgium, 11–15 September 2022.

Abstract

Re-entry flights of reusable first or upper stages typically foresee phases in the hypersonic flight regime, characterized by severe aero-thermal loads which could become critical for the most exposed components, like the vehicle forebody or the fin leading edges. These require consequently dedicated thermal protection systems (TPS), whose design generally requires a multi-disciplinary approach. In this framework, a viable solution is the use of high-temperature resistant ceramic matrix composite (CMC) structures, but the implementation of such technology, especially for the manufacturing of complex components and its application in real flight conditions, still presents significant challenges. In this work, the design activities for the CMC-based TPS of the payload forebody of a hypersonic sounding rocket are presented, developed within the framework of the STORT project, whose mission includes in flight demonstration of multiple critical technologies required for sustained flight at Mach numbers above 8, corresponding to a significantly high integral thermal load.

Keywords: ceramic matrix composites; thermal protection system; hypersonic flight experiment

Check for updates

Academic Editor: Ephraim Suhir

Received: 6 February 2026
Revised: 13 March 2026
Accepted: 13 March 2026
Published: 16 March 2026

Copyright: © 2026 by the authors. Licensee MDPI, Basel, Switzerland. This article is an open access article distributed under the terms and conditions of the Creative Commons Attribution (CC BY) license.

1. Introduction

High-energetic missions of atmospheric entry vehicles or spaceplanes flying in hypersonic conditions for prolonged time present big challenges especially due to the corresponding severe aerothermal loads. In fact, the flow is characterised by strong shock waves, dissipating the kinetic energy into internal energy in an extremely short distance, intense heat fluxes, heating up the vehicle external components, the high aerodynamic pressure loads and the presence of dissociated species, creating additional chemical reaction on the material surface [1].

In this context, one of the most challenging aspects in the development of these vehicles is the design of suitable thermal protection systems (TPS). Although the classic solution of an ablative TPS, which dissipates the heat through the thermochemical ablation

process of the surface material, is still widely used for many applications [2,3], this is not a viable solution in the cases in which the stability of the aerodynamic shape is needed, or for example, when full reusability is required. In those cases, the use of sophisticated structures based on ceramic matrix composite (CMC) materials is required, which provide a so-called passive heat protection, by sustaining very high temperatures at which they can radiate back most of the convective heat [4].

In particular, among the CMCs, the C/C-SiC material offers a very good potential for application in the hypersonic flight regime because of its combination of relatively low density, around 2 g/cm^3, high temperature resistance, with the typical temperature limit set above 1900 K at which there is the transition from passive to active oxidation of the material, and good thermo-mechanical properties also at high operational temperatures [5,6]. Although the C/C-SiC material was first produced already a long time ago [7], the research on the topic is still widely active for what concerns, for example, the use of different raw materials [8,9], the possible manufacturing processes [10,11], the modelling and characterization of the material properties and the testing of the thermo-mechanical behaviour under representative operating conditions [12].

In the context of the improvement of the readiness level of the technology, the validation under realistic flight conditions with the application of the CMC material to the design of complex TPS structures integrated in real vehicles for flight experiments assumes a fundamental role for the development. In fact, flight tests enable the characterization of real flight conditions, offsetting the limitations of ground testing while simultaneously providing data for the calibration and validation of numerical tools and models required in the design process. Among the past flight experiments foreseeing the integration of CMC components [13,14], the well-known SHEFEX I and SHEFEX II [15] are worth mentioning, in which CMC structures were integrated as TPS of the vehicle forebody for the evaluation of the thermal response in hypersonic flight conditions. Nevertheless, the mentioned flight experiments were characterized by ballistic trajectories reaching hypersonic conditions only for relatively short durations, with a consequent limitation of the integral aerothermal loads and the corresponding temperatures to which the structures were subjected. In order to achieve a longer flight duration, the STORT project was initiated by DLR, which planned a three-stage sounding rocket to fly on a suppressed trajectory, achieving a peak Mach number of more than 8 and keeping the speed above this threshold for more than two minutes. As a result, the encountered environmental conditions in terms of accumulated heat load shall be close to the ones typical of high-enthalpy re-entry flights, especially for reusable first stages, and potentially upper-stage, configurations [16].

While an overview of the STORT hypersonic flight experiment, of the setup of the three-stage sounding rocket and of the most relevant flight mission and scientific data are presented in [16], the present work focuses on the challenges characterizing the design process of the C/C-SiC-based TPS structure for the scientific payload forebody of the STORT sounding rocket. These are the components exposed to the highest thermal load and consequently require taking into consideration several engineering aspects for their full validation. Moreover, while a first technical discussion of the main engineering aspect of this process were presented in [17,18], the present work reports a systematic, complete and scientifically rigorous description of the design. In particular, starting from the planned nominal flight trajectory and the main requirement to have an axisymmetric smooth aerodynamic surface with minimized segmentation and without disturbances due to rivets or bolted connections, in order to reduce drag and avoid local heat flux increases, the paper will describe first the main design choices, in terms of the segmentation, the selection of the C/C-SiC shells manufacturing process through wet filament winding of the fibres and the selected configuration for the connection between the hot external TPS and the inner

cold structure. Then, the numerical models for the thermal analysis and the mechanical validation of the structure under the most critical load cases expected during the mission and the corresponding results will be presented. Finally, a detailed and critical comparison of the in-flight measured temperature profiles in some significant points of the structure will be compared to the corresponding numerical results for a partial validation of the numerical model and the identification of improvement possibilities.

2. STORT Sounding Rocket Configuration and Planned Trajectory

As mentioned above, the DLR project STORT focused on several key technologies for flight at prolonged time at hypersonic Mach number, with the main aim to foster reusability of the systems and to support cost reduction of future space transportation systems while keeping them highly reliable.

In this framework, a big part of the project activities was focused on the definition, implementation and carrying out of a flight experiment in the hypersonic flight regime for a relatively long operational time, in order to increase the corresponding integral aerothermal load as much as possible. For this purpose, a three-stage sounding rocket configuration was defined, as shown in Figure 1, including the S31 rocket as first stage, the S30 as second stage and the Improved Orion rocket as an engine of the third stage. Figure 2 shows the details of the third stage configuration with the scientific payload, including the C/C-SiC structure for the forebody thermal protection, which is the subject of the present paper.

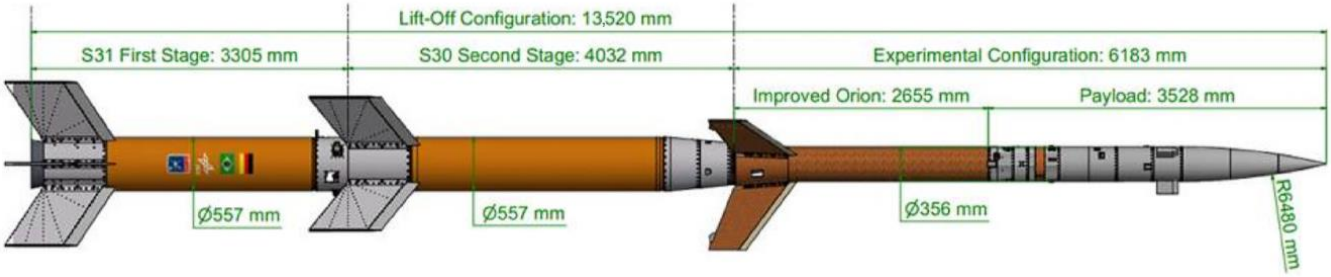


Figure 1. STORT three-stage sounding rocket configuration [16].

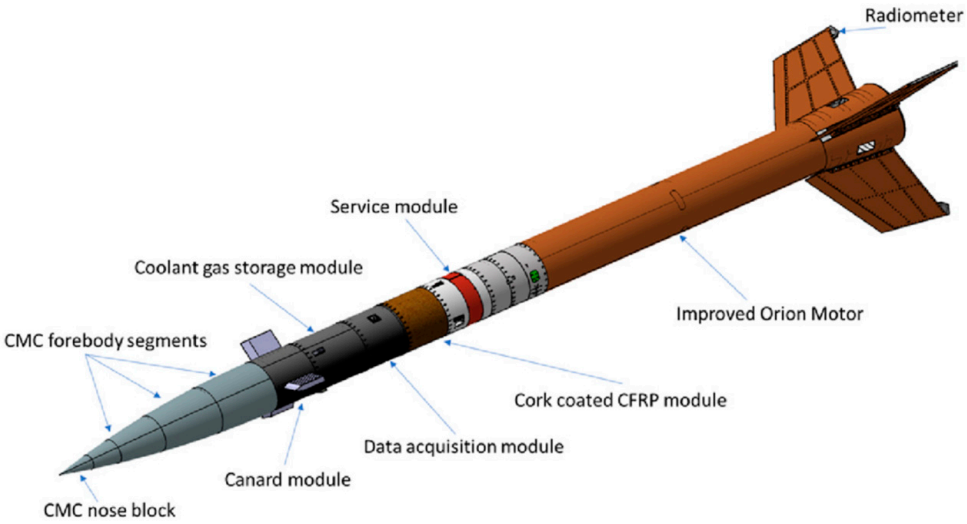
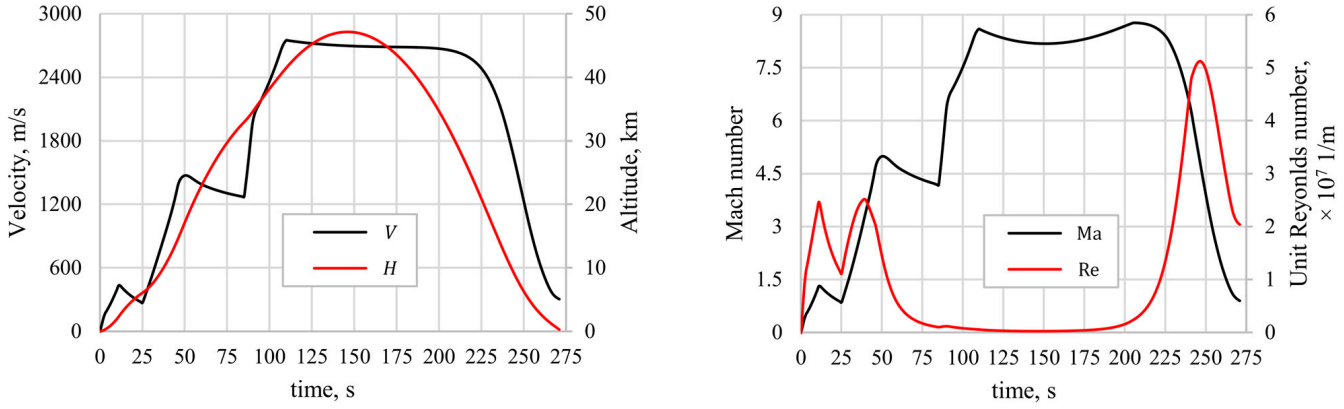


Figure 2. Upper stage of the STORT launch vehicle with scientific payloads [16].

Moreover, in order to prolong the flight time in hypersonic regime, specific manoeuvres were planned. In particular, relatively long coast phases were foreseen between the burnout of the first stage and the ignition of the second stage and between the burnout of the second stage and the ignition of the third stage, during which the rocket would perform a gravity

turn adjusting the flight direction to a lower flight path angle. The resulting planned nominal trajectory is shown in Figure 3, in terms of velocity and altitude (Figure 3a) and Mach and Reynolds numbers (Figure 3b) over time. It can be seen that the rocket was expected to fly at a Mach number around 8 for an overall time of 110 s. In Table 1, the key flight events are reported, in particular, for what concerns the motors ignition and burnout times.



(**a**) (**b**)

Figure 3. Planned nominal trajectory of the STORT flight [16], in terms of: (**a**) flight velocity and altitude; (**b**) Mach and Reynolds numbers.

Table 1. Characteristic flight events and their corresponding times [16].

Event	Time, s
Lift-off, ignition 1st stage	0
Burnout 1st stage	11.4
Ignition 2nd stage	24.0
Burnout 2nd stage	51.1
Ignition 3rd stage	88.0
Burnout 3rd stage	113.0
Apogee	141.9
Impact	265.4

An overview of the STORT sounding rocket configuration, with additional details concerning the several technologies implemented on the scientific payload, the mission definition and operation and the main selected flight data can be found in [16,18].

3. Design Overview

3.1. Forebody Structure Concept

In this section, an overview of the overall design of the 1.5 m long rocket scientific payload forebody structure with its TPS will be presented, which is schematically shown in the section view in Figure 4.

On the base of the experience collected in the previous SHEFEX II program, where a temperature increase at the edges of the faceted TPS structure of the forebody was detected, due eventually to a localized increase in the heat fluxes [15], a critical requirement defined in the case of STORT for the TPS design of the forebody was to obtain a smooth ogival aerodynamic surface, reducing the segmentation and minimizing geometrical disturbances and gaps. This requirement had a primary effect on the design choices regarding the manufacturing process and the structure configuration. In particular, the full C/C-SiC structure was divided in only five components. In the very front of the forebody, the nose

made from one solid block of material was located, featuring a tip with a spherical nose of 2.5 mm radius. The bulk design provided for a significant mass to act as a heat sink in the stagnation region. Downstream of the nose, the C/C-SiC structures are designed as axisymmetric, closed shells. The manufacturing of these structures is carried out via wet filament winding in the CFRP production and subsequent transformation into the C/C-SiC material, as detailed in Section 3.2.

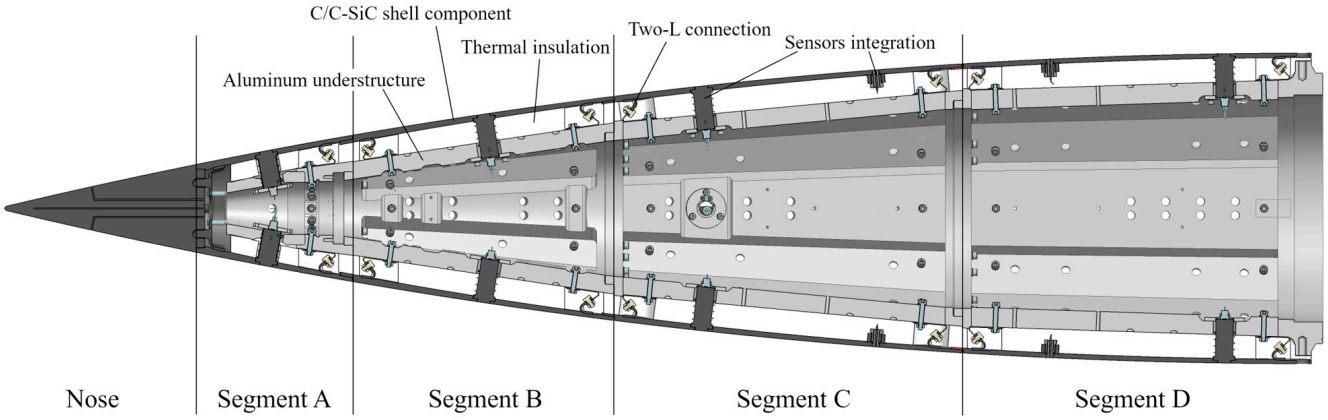


Figure 4. Cross-section of the STORT payload forebody structure.

Moreover, although gaps in the order of 1–1.5 mm were included between the shells to compensate the thermal expansion and avoid mechanical stresses between the segments, such gaps were closed with a high-temperature resistant soft graphite-based paste for keeping the external geometry neat.

The CMC segments are installed on an aluminium alloy substructure which connect the forebody to the rest of the scientific payload, fulfilling the bearing function and allowing, at the same time, the integration of sensors and other electronic hardware systems needed for the data acquisition.

A polycrystalline wool thermal insulation is included below the CMC components, preventing the energy to be conducted internally and keeping the temperature of the underlying metallic structure below the material limit.

Finally, Section 3.3 describes the connection between the CMC main components and the substructure, whose design was also defined according to the general concept of a clean external aerodynamic surface.

3.2. Wet Filament-Wound CMC Components for the TPS

The C/C-SiC components used for the payload forebody TPS were manufactured through the following process [7] involving the following steps.

- First, the raw component is set up in the carbon fibre reinforced polymer (CFRP) status.
- Second, the so-called carbon-carbon (C/C) status is generated through a pyrolysis process, at temperatures that generate the carbonization of the matrix.
- In the present case, the in-house developed in-situ joining process (see Ref. [19]) was implemented in the C/C-state to integrate ceramic brackets on the internal surface of the shell component for the connection to the substructure, according to the configuration that will be explained in details in Section 3.3.
- Finally, the C/C-SiC integral final component is realised through reactive silicon melt infiltration.

For what concerns the bulk nose component, three 30 mm thick plates were produced using carbon fibre prepregs, polymerized using an autoclave and pyrolyzed to the C/C

status. The three plates were joined and siliconized together in order to get a material block large enough to be machined to the prescribed geometry.

On the other side, as already mentioned, an innovative process was implemented for the manufacturing of closed-shell C/C-SiC components for the other segments, starting from the LSI process described above, but using the wet filament winding of pre-impregnated carbon-fibre bundles for the production of the initial CFRP preform.

This process is best suited for the near-net-shape production of rotationally symmetric components, like the forebody segments in the present work. In this process, a single carbon fibre roving is first impregnated with the phenolic resin in a resin bath and then placed on the winding core, which determines the inner contour, through computer control. Once the winding is complete, curing normally takes place directly on the winding core at prescribed temperature in drying ovens or in an autoclave.

Important factors that influence the material properties of wound ceramic matrix composites are the choice of the winding pattern and of the winding angle relative to the winding axis [10,20]. The winding angle should be adapted to the existing load cases but also needs to be varied over the wall thickness to obtain an even and delamination-free structure. In this specific case, an average winding angle of 45° was chosen, which is best suited for the combination of radial and axial loads. For segment A, this results in angles between 40° and 55°, for segment B, 36° to 67°, for segment C, 36° to 62° and for segment D, 39° to 54°. CADWIND® was used to generate the winding programs of the forebody components. The 6th winding layer of segment B generated by CADWIND can be seen in Figure 5.

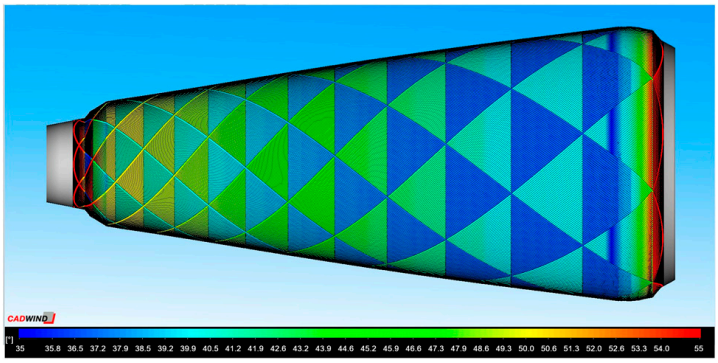


Figure 5. Sixth winding layer of segment B in CADWIND®.

The T800 carbon fibre from Toray Industries (Tokyo, Japan) was used in combination with a phenolic resin with the internal name JK60. This combination has been established for wound C/C-SiC structures at DLR. In order to achieve the desired component minimum wall thicknesses of 5 mm, 12 winding layers were required for all segments. Nevertheless, the segments were produced with a small amount of extra material on the outward surface to machine the outer contour to the final shape in the C/C condition.

3.3. Connection Elements Between TPS and Substructure

The design of the connection between the CMC components and the metallic substructure represented one of the most significant challenges, since it needed to take into account all the following requirements.

First, the general requirement of avoiding disturbances on the external aerodynamic surface was also applied here and required that no bolt or rivet heads were present on the surface. Therefore, the in-situ joining technique was selected [19] to attach bracket elements on the segments' internal surface. As mentioned before, this step can be applied when there are two components in the intermediate C/C status which need to be attached together.

This can be achieved using a carbonaceous paste that after tempering assumes a similar porous state as the C/C material. The C/C components are pressed together, using the paste as an adhesive, and infiltrated with molten silicon. The infiltration overcomes the joining interface and yields a final integral C/C-SiC component. A consequence of this choice is that the connection elements should include a bracket also made from the same CMC material.

On the other side, the connections must fulfil the primary functions of bearing different types of mechanical and thermal loads and providing a compensation of thermal expansion mismatch between the high temperature experienced on the external components to the near-ambient temperature of the metallic ones. In the case of the thermo-mechanical loads arising during the STORT flight mission, it was proved that a purely CMC connection would not be able to provide the needed mechanical resistance, as described in details in the technical trade-off study presented in [17].

Therefore, the connection between the C/C-SiC structures on the surface and the internal metallic structure was realized via the so-called double-L connection, as shown in Figure 6. This design is a refinement of the connection elements that were used in the SHEFEX II vehicle, that consisted only of CMC material and were made in one piece [15]. The design of the double-L connection consists of two parts, the one being a CMC angled bracket which is joined to the TPS shell, the other one being a metallic angled bracket that is attached to the CMC bracket and to the metallic substructure via bolts. The material of choice for the bracket and the bolts was Inconel 600. This design is quite simple in terms of the two parts required, and, more important, it provides elasticity in the metallic bracket which reduces the mechanical stress in the CMC bracket, and it gives the possibility to adjust for tolerances in the assembly process.

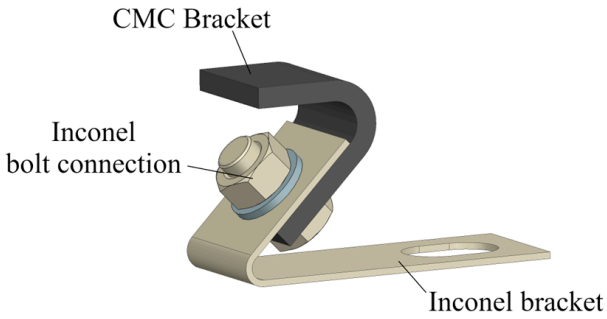


Figure 6. Two-L connection concept.

Figure 7 shows the implementation of the two-L connections for the overall assembly of the TPS shell to the underlying structure for the example case of segment B, including 12 elements in the proximity of the front section and 12 elements in the proximity of the rear section. A similar configuration was used for the segments C and D.

Figure 8 presents, finally, the distinct configuration for the assembly of the nose to segment A, which requires dedicated treatment. In this case, in fact, on the forward part, a special configuration was needed, in which an additional CMC disc component is included to the segment A through the above described joining process, which presents four holes through which four ceramic M10 screws ensure the connection to threaded holes eroded in the tip. An overview of the CMC screw connection and their effectiveness can be found in [21]. Moreover, the tilting movement between the TPS and the metallic structure is avoided through four dowel pins bolted on the front face of the substructure and passing through the CMC disc. On the rear side of the segment A, the two-L connection elements could be still applied, but to allow the sensor integration, only 10 instead of 12 junctions are implemented.

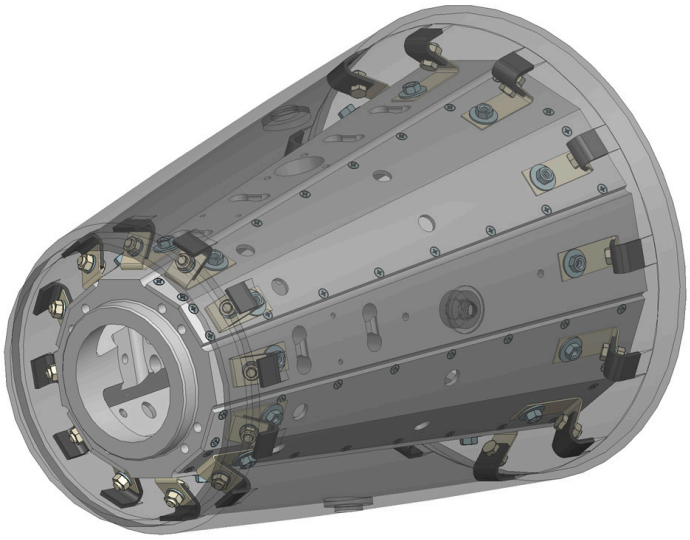


Figure 7. Configuration for the connection between TPS shell and substructure, for the example case of segment B (the thermal insulation is hidden for clarity).

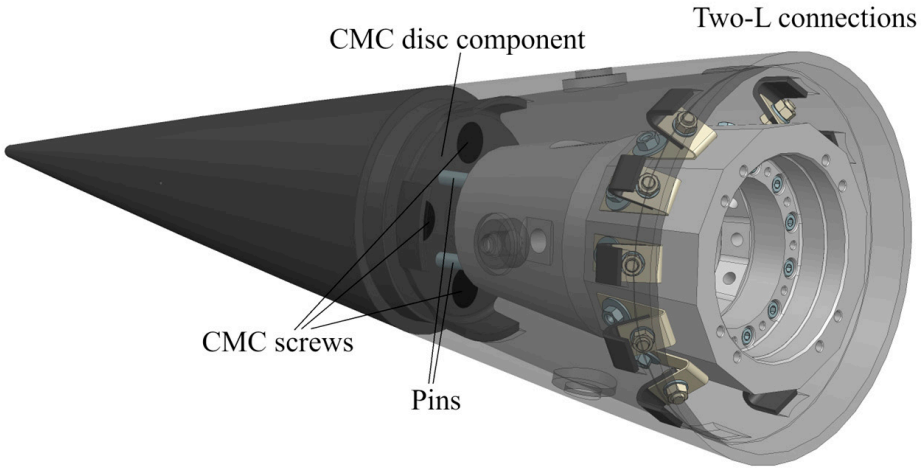


Figure 8. Configuration for the assembly of the nose and segment A.

4. Numerical Analyses for the Thermo-Mechanical Validation of the Structure

In this section, the numerical model and the corresponding results for the thermal and mechanical validation of the forebody structure with its TPS will be presented.

4.1. TPS Thermal Analysis

Numerical model for the thermal analysis

As already discussed, one of the main challenges that the hypersonic flight presents is the corresponding very high-energetic flow developing around the external surface. Therefore, the definition and implementation of a suitable numerical model that allows to predict the corresponding thermal load and consequently the thermal response of the structure during the flight plays a fundamental role in the design process.

Here, a relatively simplified model is proposed that aims to fulfil the above-described objective without requiring high computational time and resources, so that it can be used also for parametric studies and several kinds of analyses during the design phase.

The numerical simulations were carried out using the ANSYS Mechanical simulation environment, performing a transient thermal analysis via the Finite Elements method (FEM). The model included the TPS shell structures and the high-temperature thermal insulation.

The applied boundary conditions were:

- A convective heat flux $\dot{q}_c$ on the shell surfaces, given by the following equation

$$\dot{q}_c = h(T_r - T_w) \quad (1)$$

with h being the heat transfer coefficient, T_r the recovery boundary-layer temperature and T_w the wall temperature.

- A radiation heat flux from the shell external surfaces to the environment, using an emissivity of 0.85 for the CMC material, as a typical average value from literature data [22].
- Thermal contact between the shells and the high temperature thermal insulation.
- Adiabatic condition on the inner surfaces of the thermal insulation and model sides.

A simplified approach is assumed here for a fast estimation of the convective heat flux on the external surface. The surface is divided into different areas according to the design of the forebody. It considers the half-sphere of the tip for the stagnation region and in the following the surfaces of the rest of the nose and those of the downstream segments. The surface divisions are treated as linear objects for a simplified approach which is depicted in Figure 9 (the figure is not in scale to magnify the approximation in the linearization). For each division, a 1D analytical flow field calculation for the known payload forebody geometry and the assigned nominal trajectory is considered. In particular, in the continuum regime, which is a valid assumption considering that the nominal apogee, is around 47 km; from the assigned nominal altitude H, the ambient pressure p_∞ and temperature T_∞ can be obtained assuming the U.S. standard atmosphere model (COESA76) [23]. Assuming ideal gas behaviour, from the nominal velocity V_∞, the flight Mach number Ma_∞ can also be calculated. Furthermore, once supersonic flight is reached, the fluid dynamic conditions for each segment can be calculated as the conditions downstream either the conical shock wave or the expansion fan forming at each geometrical inflection (see Figure 9). In this work, the approximate solution proposed in [24] is implemented for solving the conical shock wave, while the classical Prandtl–Meyer [1] expansion model is used for solving the expansion fans. For the stagnation region, which is treated separately, the classical model for normal shock waves is used [1]. In the subsonic regime, at the beginning and at the end of the trajectory, constant conditions are considered, while in the transonic regime, a linear interpolation is assumed; by having these two phases, a relatively small effect on the results of the thermal analysis. Finally, Sutherland's law is considered for the estimation of the dynamic viscosity μ and the thermal conductivity λ [25].

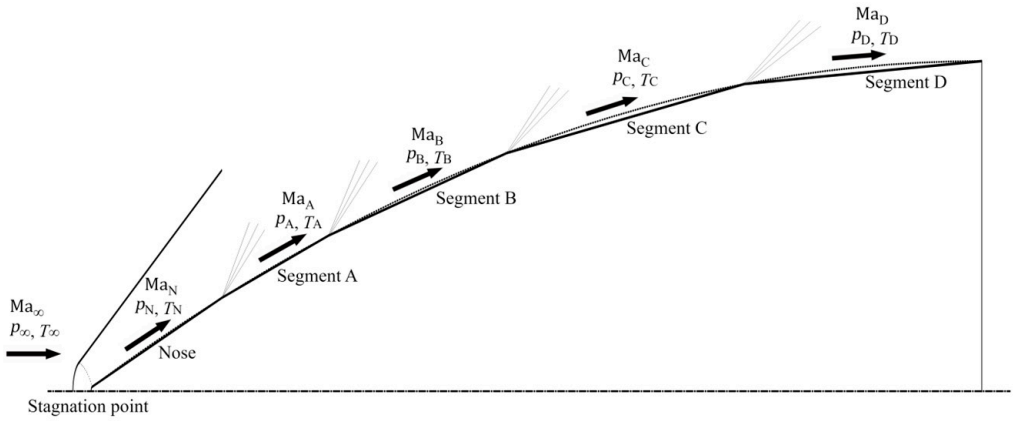


Figure 9. Schematic representation of the simplified 1-dimensional evolution of the supersonic flow around the STORT forebody (not in scale).

Assuming constant conditions at each of the mentioned regions, suitable classic correlation formula are applied for the calculation of the heat transfer coefficient h.

In the stagnation region, the correlation following [26] is considered:

$$h = 0.763\ \mathrm{Pr}_{\infty}^{-0.6}\sqrt{\frac{V_{\infty}}{R}\rho_{\infty}\mu_{\infty}\ f(\mathrm{Ma}_{\infty},\gamma)}\ c_p \tag{2}$$

where ρ_{∞} and μ_{∞} are the flow density and dynamic viscosity, c_p is the specific heat at constant pressure, γ is the specific heat ratio, $\mathrm{Pr}_{\infty} = \frac{c_p\mu_{\infty}}{\lambda_{\infty}}$ is the Prandtl number and R is the tip radius.

The heat flux coefficient present on the shell structures was estimated as:

$$h = \mathrm{St}\ \ c_p\ \rho\ V \tag{3}$$

In addition, with the correlation for laminar flow over a flat plate of length L, whereby the Mangler transformation [27] was applied to account for the fact of the shells being axisymmetric bodies of revolution, to yield the Stanton number St as:

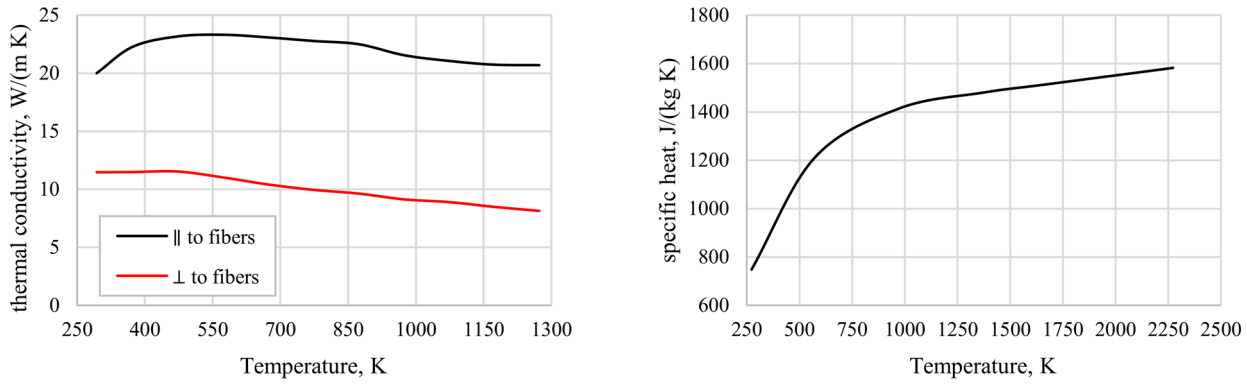
$$\mathrm{St} = \sqrt{3} \times 0.664\ \mathrm{Pr}^{-\frac{2}{3}}\ \mathrm{Re}_L^{-\frac{1}{2}} \tag{4}$$

where $\mathrm{Re}_L = \frac{\rho V L}{\mu}$ is the Reynolds number. Although the hypothesis of laminar flow is a strong simplification that could lead to significant errors in case of turbulent flight regime, in case of the STORT flight, it is justified considering the expected nominal unit Reynolds number, as shown in Figure 3b. This, in fact, reaches a relatively high value (above $5{\cdot}10^6$ 1/m) only in the initial phase of the flight, where the Mach number is still relatively small, and in the final phase. Therefore, the flow was expected to be laminar for the large part of the flight in hypersonic conditions. Further consideration about the validity and the limits of such hypothesis are discussed in Section 5 on the basis of the comparison between numerical results and flight data.

The recovery boundary-layer temperature on the other hand is calculated as:

$$T_r = T\left(1 + \sqrt{\mathrm{Pr}}\frac{\gamma - 1}{2}\mathrm{Ma}^2\right) \tag{5}$$

Finally, for the FE thermal analyses, an orthotropic model for the C/C-SiC components is assumed, with a density of 1900 kg/m^3 and temperature-dependant specific heat and thermal conductivities in both the in-plane and the normal directions, as reported in [28] and shown for the sake of completeness in Figure 10.



(**a**) (**b**)

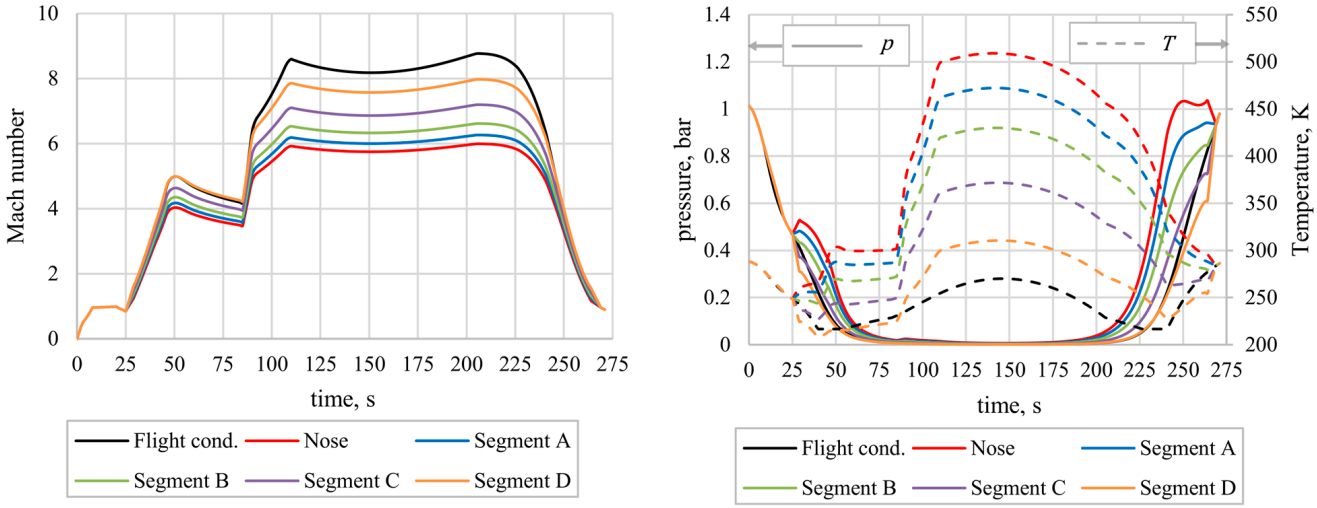
Figure 10. C/C-SiC thermal properties: (**a**) thermal conductivity; (**b**) specific heat.

For the polycrystalline insulation, a density of 120 kg/m^3 is considered, taking into consideration the fact that the wool is compressed between the CMC shells and the aluminium structure, and the thermal properties as per catalogue are considered [29].

4.2. Results of the TPS Thermal Analysis

Here, the results of the above-described numerical model applied to evaluate the TPS structure thermal response given the planned nominal trajectory shown in Figure 3 are presented.

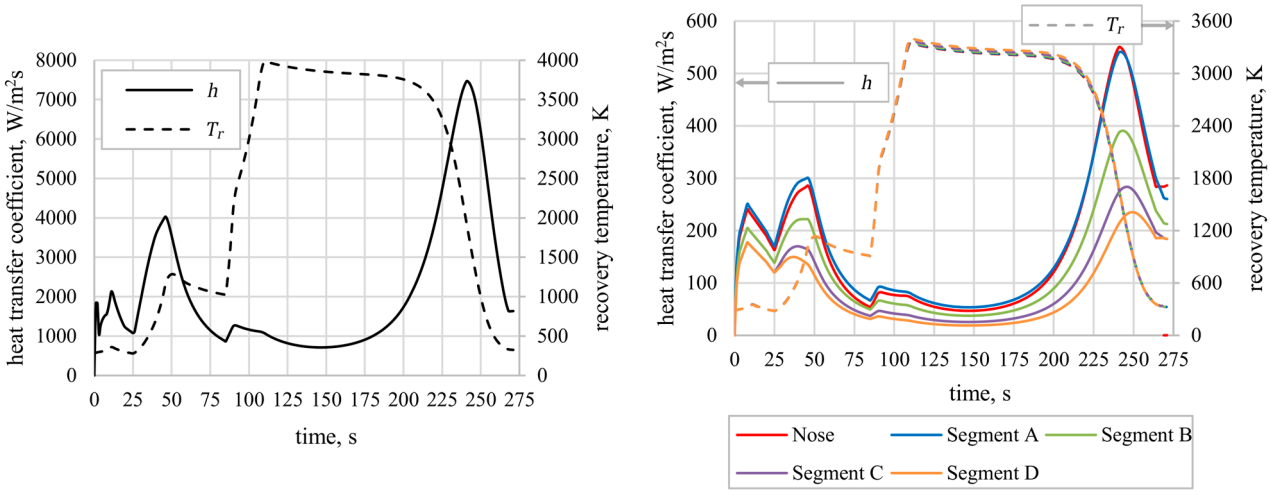
First, Figure 11 shows the flow conditions around the different segments of the STORT forebody as estimated with the 1D model described in the previous section. According to the considered schematic evolution of the flow as shown in Figure 9, the flow Mach number has first a drop downstream the shock wave forming in front of the nose and then it gradually increases due to the following expansions. Correspondingly, static temperature and pressure have a qualitative opposite behaviour.



(**a**) (**b**)

Figure 11. 1D estimation of the flow conditions around the forebody segments, in terms of: (**a**) Mach number; (**b**) temperature and pressure.

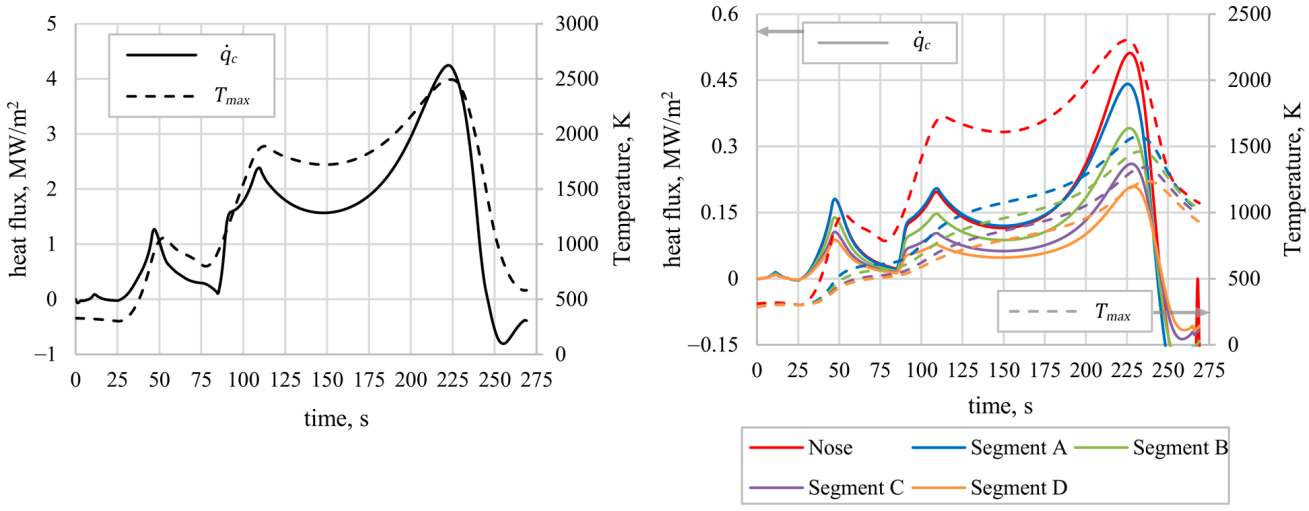
From the estimation of the flow conditions, the heat transfer coefficient can be calculated with Equation (2) for the stagnation point, as shown in Figure 12a, and with Equations (3) and (4) for the other areas, as shown in Figure 12b. Moreover, the recovery temperature is calculated with Equation (5), which is also displayed in the same graphs. It can be noticed that the heat transfer coefficient presents a significant increase for all the areas during the burning of the first two stages and a corresponding decrease during the coast phases. Then, a small increase can also be noticed during the third stage operation, followed by an almost constant value during the flight at high altitudes. Finally, the coefficient grows during the high-velocity descent reaching a maximum value and then decreases due to the vehicle deceleration. The profiles of the recovery temperature on the other side follow the trend of the Mach number, with a slight difference between the different areas due to the change of the transport properties and, consequently, of the Prandtl number.



(**a**) (**b**)

Figure 12. Estimation of the time profiles of the heat transfer coefficient and recovery temperature on the external surface of each TPS region for: (**a**) the stagnation point; (**b**) the other segment surfaces.

With the above described quantities set for the convection boundary conditions on the forebody external surface, the FE thermal analysis was performed and the results are shown in Figure 13, in terms of the time profiles of the convective heat flux and of the maximum wall temperature for each segment, and in Figure 14, in terms of the calculated temperature distribution on the TPS at t = 220 s, i.e., around the time when the maximum value of the temperature at the stagnation point is reached.



(**a**) (**b**)

Figure 13. Calculated time profiles of the maximum temperature and of the convective heat flux on the external surface of each TPS region for: (**a**) the stagnation point; (**b**) the other segment surfaces.

In particular, the profiles of the convective heat flux qualitatively follow the trend of the heat transfer coefficient, with the difference that the heat flux stays on a relatively high value for the whole duration of the flight at Mach number 8, because of the high value of the recovery temperature. Nevertheless, the convective heat flux profiles also reach a peak between 220–230 s, with a maximum value of around 4 MW/m^2 at the stagnation point and between 0.2–0.5 MW/m^2 on the other segments. Correspondingly, the maximum

temperature profiles for the different regions reach also a peak around the same times, with very high values at the stagnation point and in the surrounding surface.

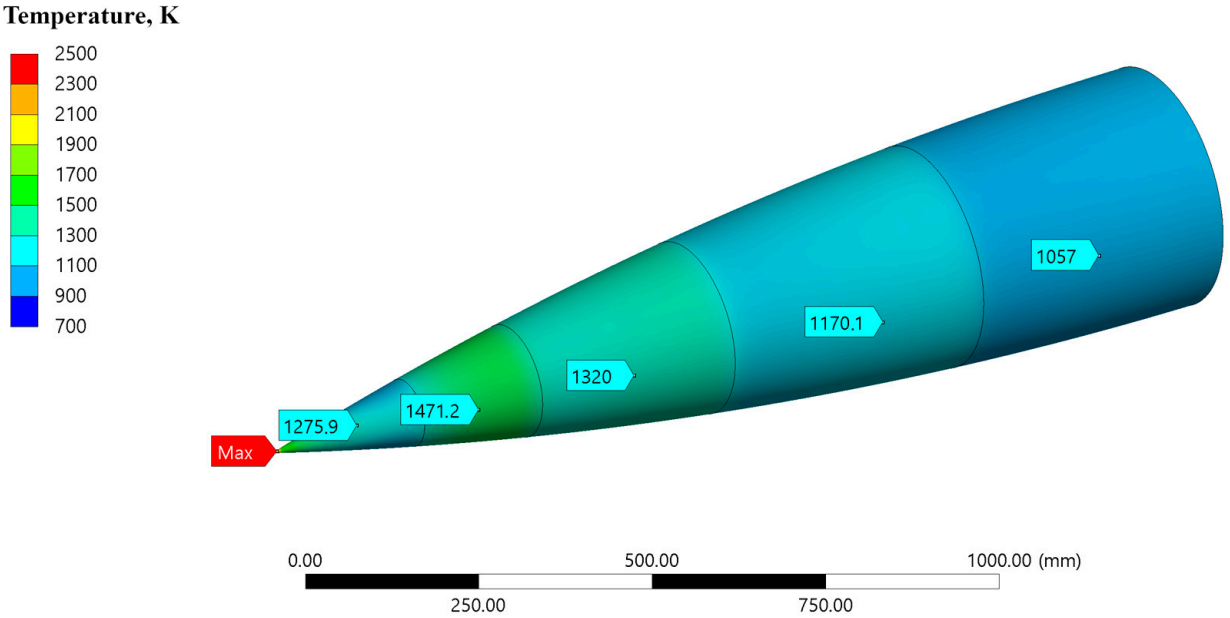


Figure 14. Simulated temperatures on the TPS at time of t = 220 s.

A specific effect is expected to occur approximately at the time of t = 180 s, when the tip temperature is predicted to reach and surpass 1900 K. At roughly this temperature, the oxidation behaviour of the C/C-SiC material could change from passive to active oxidation, depending on the pressure conditions. Thereby the mass loss rate due to oxidation would increase considerably and the tip radius would also change, with a subsequent reduction effect on the convective heat flux according to Equation (2). However, considering the results shown in [30], which shows the erosion rates measured during previous laboratory tests for the same C/C-SiC material for a wide range of conditions, the erosion rate at the nose tip is expected to be on the order of 10^{-2} kg/(m^{2}s) when the abovementioned temperature limit of 1900 K is reached. Considering that this phenomenon interests a maximum area extension of 1 cm^2 for a maximum duration of around 60 s, we can expect a maximum mass loss of 0.06 g that can be considered negligible for the STORT flight. The downstream CMC structures do not see temperatures that come close to the transition temperature and stay between 1200 to 1500 K.

Other important information for the structure design that could be obtained from the described thermal simulation include the temperature on the thermal insulating polycrystalline wool inner surface, that is at its interface to the inner aluminium structure, as shown in Figure 15. Here it can be noticed that the temperature on the insulation inner surface stays quite low for the whole flight duration, except that in the most forward region on segment A, where it is expected to increase above 450 K at around 240 s, which is the temperature at which the loss of the mechanical strength of aluminium alloy is 25% [31].

Moreover, the temperature distribution calculated for the TPS represents also a critical load for the structure, because of the corresponding thermal expansion of the material, which in the present case, where the structure is made of close axisymmetric shells, significantly affects the stresses in the connection elements. This has been properly taken into consideration as it will be shown in the next section.

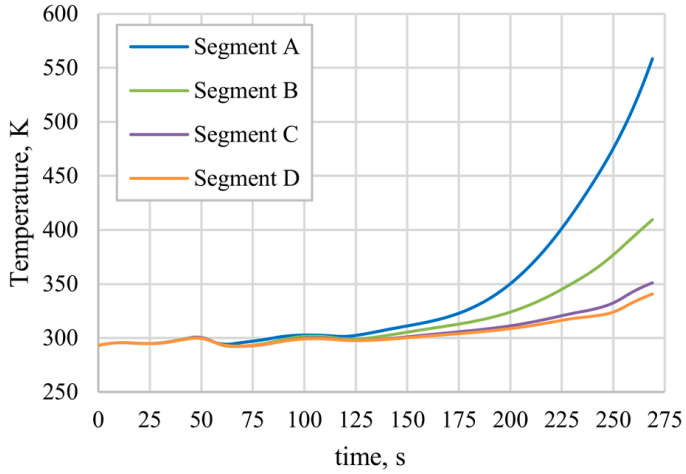


Figure 15. Average temperature on the thermal insulation polycrystalline wool inner surface.

4.3. Forebody Structure Mechanical Validation

For the sake of completeness, the FE static mechanical simulations carried out with the ANSYS Mechanical 2020 R2 software for the forebody structure mechanical validation are presented in this section.

The different segments of the forebody were analysed separately, based on the justified assumption that there is no significant interaction between them in terms of mechanical behaviour. Each segment model contained the internal metallic structure, the high-temperature insulation and the CMC shell structure including the CMC and metallic connection brackets with bolts and nuts. The metallic substructure was given a fixed boundary condition at its back interface. The CMC connection brackets were affixed to the CMC shell by bonded contacts, whereas the bolt connections were treated with detailed modelling of the frictional contacts, with a friction of coefficient of 0.2, including also the pretension of the screws of 4500 N.

Also in this case, an orthotropic material model is assumed for the C/C-SiC shells, with the material elastic properties taken from [32] for the case with $\pm 45^{\circ}$ fibre orientation. For the coefficient of thermal expansion (CTE) the temperature-dependent data shown in Figure 16 was implemented.

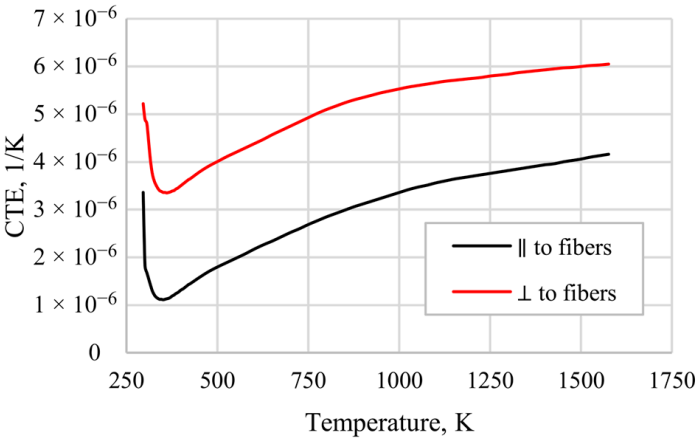


Figure 16. Temperature dependent coefficient of thermal expansion for the C/C-SiC material.

Different load conditions were simulated, representative of the critical loads expected during the flight mission. In this work, only the most critical load case is presented in detail, given by the combination of the thermal and the aerodynamic pressure loads. In particular, the aerodynamic pressure load was determined through computational fluid

dynamic simulations of the STORT payload in different points of the trajectory for different possible angles of attack. Among the considered cases covering the most critical points in the planned trajectory, the highest pressure load was calculated for the flight conditions t = 217.9 s at the conservative case of an angle of attack of 10°, as shown in Figure 17. The combination of the presented asymmetrical pressure load, interpolated on the surface of each segment and the corresponding temperature distribution calculated with the thermal analysis shown in Section 4.1 at the same time t = 217.9 s was considered for the mechanical simulation of each individual segment.

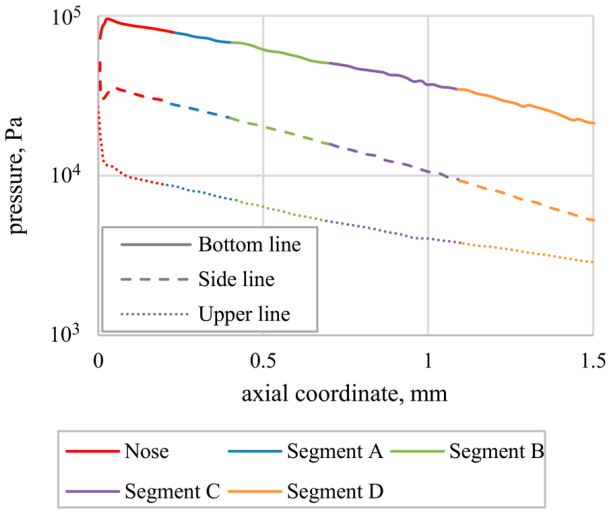


Figure 17. Simulated pressure over the forebody at time t = 217.9 s (angle of attack of 10°).

The resulting overall deformation is shown in Figure 18 for the example of segment B (the thermal insulation is omitted to highlight the behaviour of the connection elements). In this case, the load is clearly non-axisymmetric, and the connection elements are subjected partly to compression and partly to tension.

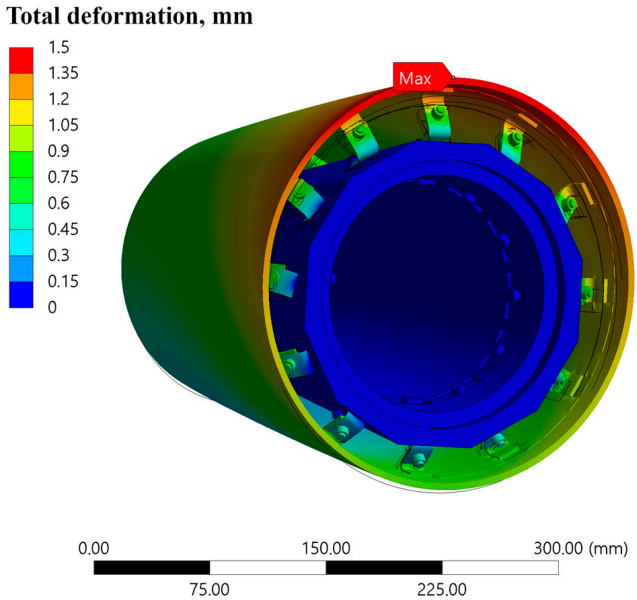


Figure 18. Deformation of segment B as result of combined pressure and temperature load.

Figure 19 shows the corresponding distribution of the maximum principal stress in the CMC and in the Inconel brackets of the connection element, for which the maximum stress is encountered. In particular, it can be noticed that the chosen two-L configuration

allows to reduce the stress in the CMC element, below the limit of the C/C-SiC material, whose bending maximum stress is around 180 MPa, thanks to the flexibility introduced with the thin Inconel bracket. The Inconel bracket is correspondingly subjected to relatively higher stress, but still low compared to the material maximum stress (for the Inconel 600 the maximum stress is in the range 550–690 MPa).

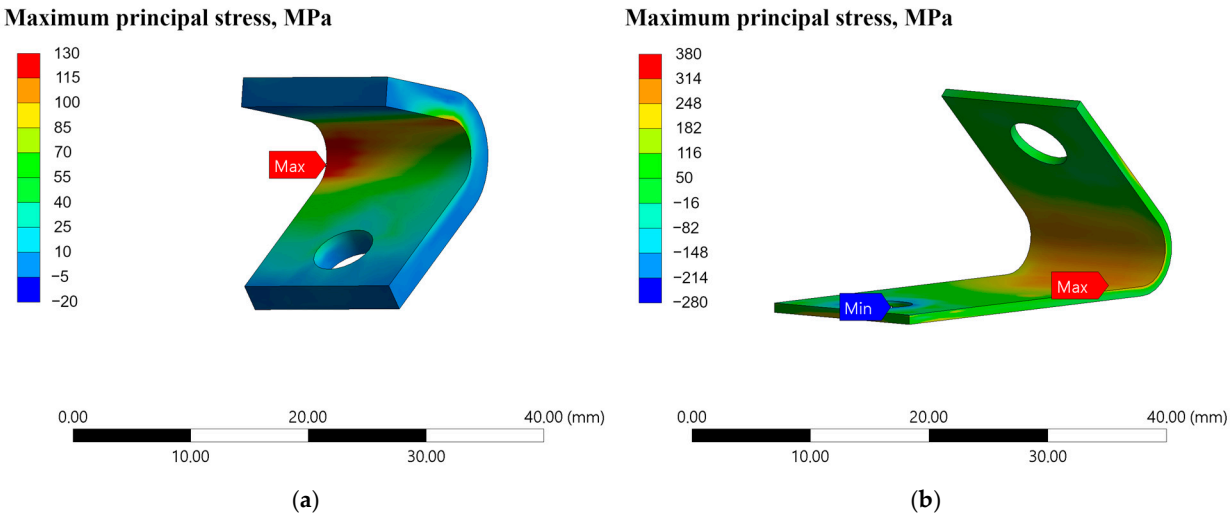


Figure 19. Maximum principal stress distributions in the connection element for: (**a**) CMC bracket; (**b**) Inconel bracket.

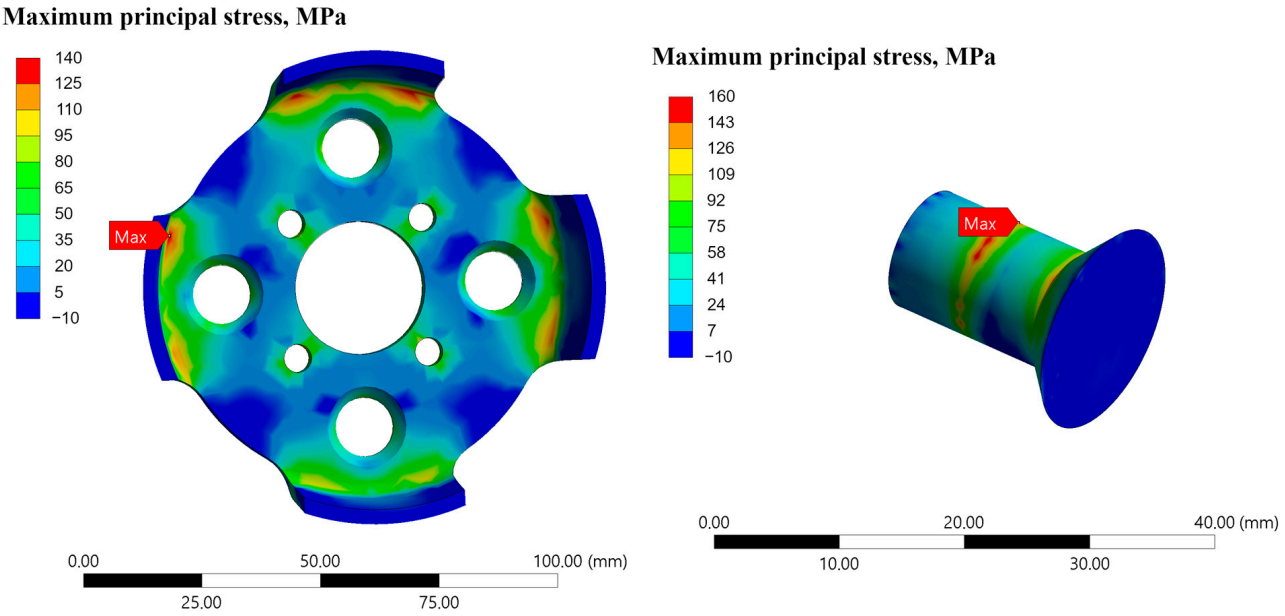
While the corresponding results obtained for segments C and D show qualitatively a similar behaviour as the ones shown above, a special case is given by the assembly of nose and segment A, which in this case, are directly connected to each other and needed to be considered together. In this case, in the section between nose and segment A, the thermo-mechanical load is transferred to the CMC disk element and screws (see Figure 8), resulting in the stress distribution shown in Figure 20. It can be noticed that although the maximum principal stress reaches a relatively high value, it is also still below the material limit in the conservative load case considered here.

Finally, the main results for the different segments are reported in Table 2. The stresses in the C/C-SiC shells and in the aluminium structure are relatively low for all cases. The last row of Table 2 shows the maximum stress ratio, calculated as the ratio between the calculated maximum stress and the CMC allowable stress, from which it can be seen that the safety margin in the CMC components is always higher than 10%.

Table 2. Static mechanical simulation results for the case of the critical combination of pressure and thermal load.

	Segment A	Segment B	Segment C	Segment D
Maximum axial displacement, mm	0.76	0.88	1.09	0.56
Maximum radial displacement, mm	0.52	1.27	1.51	1.20
Max. stress in CMC element, MPa	110.1 [a] 137.0 [b] 156.7 [c]	127.9 [a]	147.5 [a]	121.4 [a]
Max. stress ratio in CMC element	0.61 [a] 0.76 [b] 0.87 [c]	0.71 [a]	0.82 [a]	0.67 [a]

[a] For the CMC bracket in the connections between TPS shell and aluminium structure [b] For the CMC disk connection between bulk nose and TPS shell [c] For the CMC screw.



(**a**) (**b**)

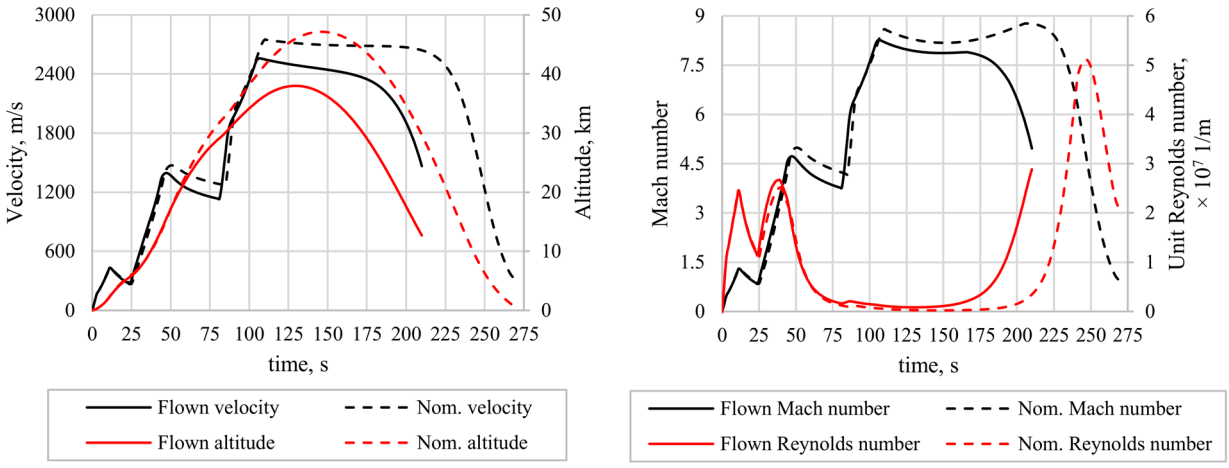
Figure 20. Stress distribution in the CMC components connecting forebody bulk nose and segment A: (**a**) disk element; (**b**) screws.

5. Comparison Between Thermal Analysis Numerical Results and Flight Temperature Data

Finally, in order to have a partial validation of the numerical model used for the thermal analysis of the rocket payload forebody structure, a numerical simulation was performed considering the real flown flight trajectory and the corresponding numerical results are compared with the in-flight measured temperatures.

A detailed overview on the STORT launch campaign and some selected flight data can be found in [16]. For the sake of completeness, here, the flown trajectory in terms of altitude, velocity and Mach and unit Reynolds numbers profiles is shown in Figure 21, also in comparison with the planned trajectory. Here, it can be noticed that the actual time of flight at Mach number around 8 was shorter than planned, due to a mistakenly delayed ignition of the third stage, which determined a flight at lower altitudes with higher aerodynamic drag force leading to stronger deceleration of the vehicle.

Furthermore, the nominal positions of the thermocouples integrated in the forebody CMC components are shown in Figure 22, from which the experimental data shown in the following are obtained. In particular, two type S thermocouples (TS001 and TS002) and two type K thermocouple (TS003 and TS004) were integrated in the bulk nose (see Figure 22a), although it must be mentioned that the thermocouple TS001 was damaged, probably during the integration, and delivered no data during the flight. For what concerns the shell components, four type K thermocouples were integrated at each of the axial positions shown in Figure 22b, separated by 90° in the azimuthal coordinate, with a nominal distance from the external surface of 2 mm. In addition, computer tomography scans were performed after the thermocouples integration to determine each sensor's exact position.

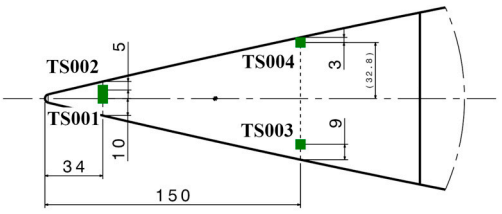


(**a**) (**b**)

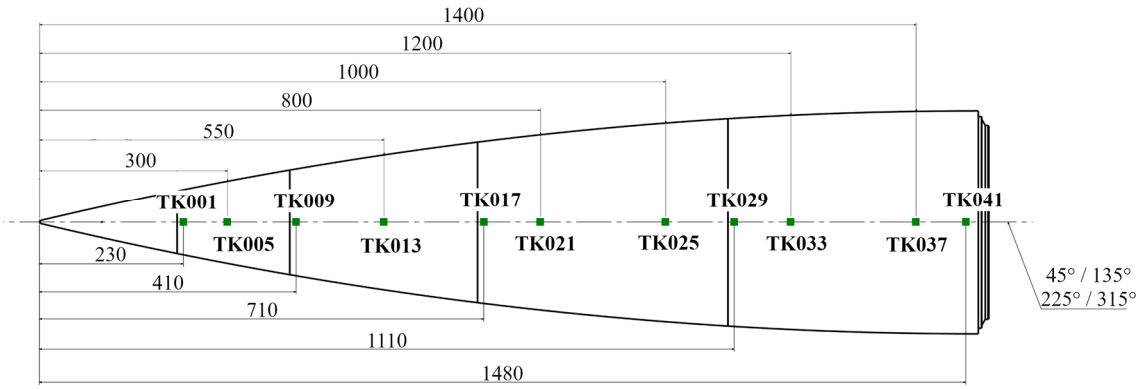
Figure 21. Planned and flown altitude and Mach number of the STORT sounding rocket, in terms of: (**a**) flight velocity and altitude; (**b**) Mach and Reynolds numbers.

Figure 23 shows the comparison between the in-flight measured temperatures at the most significant example points and the corresponding numerical results obtained with the model described in Section 4.1 for the flown trajectory data at the same locations of the selected thermocouples. Table 3 reports the corresponding normalized root mean square deviation (NRMS) calculated as:

$$NRMS = \frac{\sqrt{\frac{1}{n}\sum_{i=1}^{n}\left(T_{num,i} - T_{exp,i}\right)^2}}{T_{exp,max} - T_{exp,min}} \quad (6)$$

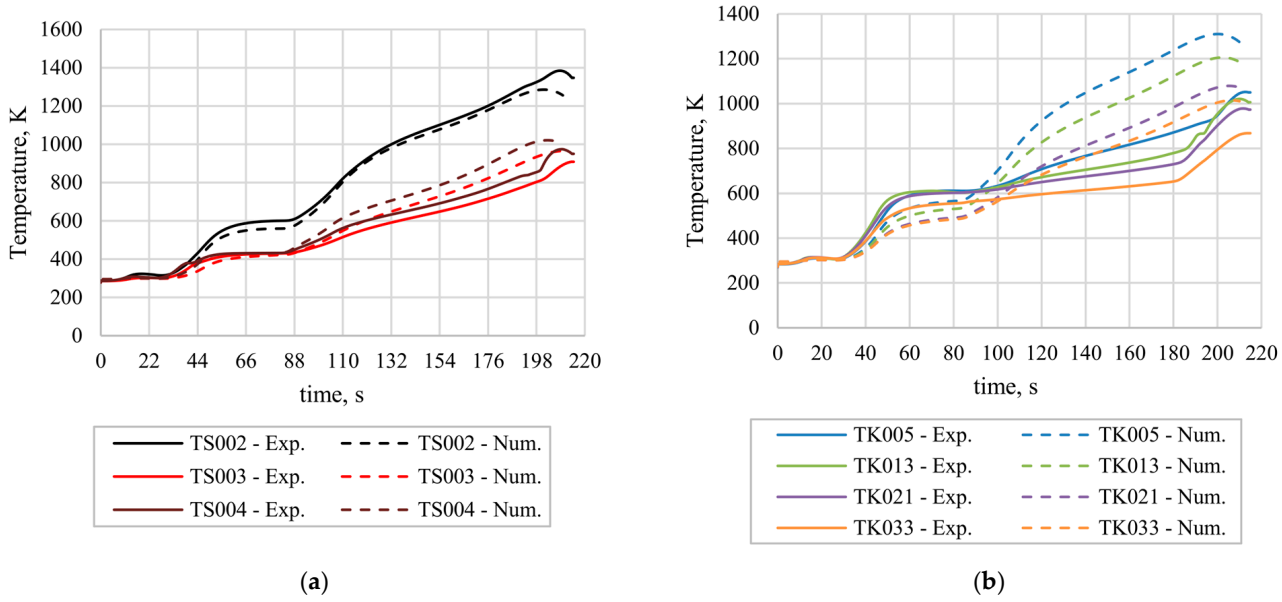


(**a**)



(**b**)

Figure 22. Positions of the thermocouples integrated in the STORT sounding rocket forebody, in particular: (**a**) in the bulk nose; (**b**) in the CMC shell segments (name tags referring to the 45° line).



(**a**) (**b**)

Figure 23. Comparison between the in-flight measured temperature data and the corresponding numerical results for: (**a**) nose; (**b**) shell segments.

Table 3. Normalized root mean square deviation between flight data and numerical results.

Thermocouple ID	CMC Component	NRMS
TS002	Nose	0.06
TS003	Nose	0.14
TS004	Nose	0.12
TK005	Segment A	0.28
TK013	Segment B	0.25
TK021	Segment C	0.19
TK033	Segment D	0.24

The results show a generally satisfying agreement between the experimental and numerical profiles, especially for the temperatures of the nose (see Figure 23a).

The discrepancies between the results are more pronounced in the case of the temperatures at the shell segments, where the simplifying assumptions in the 1D estimation of the flow evolution have a more significant effect. In addition, in this case, the thermal response is also affected by the transition from laminar to turbulent flow. In particular, this phenomenon has a significant effect in the early phase of the flight, where it can be observed that the in-flight measured temperatures raise more than estimated from the numerical simulation, and in the last part of the flight, where the flight data show a change of the slope of the temperature profiles between 180 s and 200 s (to this regard, see also Ref. [33]). The described effect can be correlated with the flight unit Reynolds number, showing that the flow becomes turbulent for values above circa $5 \cdot 10^6$ 1/m, confirming the assumptions discussed in Section 4.1.

Even with the assumption of a fully laminar flow, the computed surface temperatures become higher than the values measured in the flight phase with the laminar to turbulent boundary layer transition. This could be caused by some phenomena that can impact that data and are not considered in the model, like thermal non-equilibrium of the flow, change of the surface emissivity due to the passive oxidation of the material surface, change of the thermocouple contact behaviour and so on.

In spite of these discrepancies, considering that the flow is still laminar for the largest part of the flight trajectory and noticing that the numerically predicted temperatures are

conservative, the results show the validity of the implemented model as a relatively fast tool for the structure design phase. Furthermore, as also already mentioned, the flight results of this and other similar experiments constitute an important database which helps to improve the numerical models, which is already the focus of the ongoing activities.

6. Conclusions

In the framework of the DLR project STORT, which had the aim of developing and ultimately flight-testing key technology for reusable launcher first and upper stages also in the hypersonic conditions typically encountered in the re-entry trajectory, a three-stage sounding rocket was developed to be launched on a suppressed flight trajectory, allowing to achieve a Mach number around 8 for a relatively long time. In the present paper, the design process for the forebody TPS structure is presented, based on the application of the high-temperature resistant C/C-SiC material allowing the thermal stability of the structure also under the abovementioned severe flight conditions.

In order to meet the requirement of minimizing geometrical discontinuities on the external aerodynamic surface, the 1.5 m long structure was divided in five segments, i.e., a first bulk nose followed by four axisymmetric closed CMC shell segments obtained by wet filament winding of the carbon fibre in the first step of the LSI manufacturing process. In addition, to meet the same objective of keeping the aerodynamic flow free of disturbances, the connection between the TPS shells to the internal metallic structure was realized via a specific "double-L" connection. This design provides for a CMC bracket which is joined to the inside of the TPS shell during the material processing, becoming an integral part of it and avoiding surface disturbances, and a separate metallic bracket which is allowing for the required level of elasticity to reduce the stress in the CMC bracket.

A commercial polycrystalline wool is inserted in between CMC shells and aluminium structure to provide further thermal insulation.

The proposed design was supported and validated by numerical FE simulations. In particular, a simplified model is proposed in the present paper to estimate the thermal load for the given trajectory, providing the boundary conditions for the FE analysis of the structure thermal response. Moreover, FE mechanical simulations have been carried out in a number of representative load cases, among which the combination of the temperature load and aerodynamic pressure load was assessed to be the most critical one.

Finally, the temperature measured in the CMC components during the sounding rocket flight provided an important database to have a first assessment of the validity of the proposed numerical model, which proved to be on the conservative side, while allowing on the other side to continue the ongoing activity to refine the model and increase its reliability.

Author Contributions: Conceptualization, G.D.D.M., T.R., L.D. and A.G.; Methodology, G.D.D.M., L.B. and L.D.; Validation, T.R., D.H. and A.G.; Formal analysis, G.D.D.M.; Investigation, G.D.D.M., T.R., L.B. and L.D.; Resources, L.B. and D.H.; Data curation, G.D.D.M.; Writing—original draft, G.D.D.M.; Writing—review & editing, T.R., L.B., L.D., D.H. and A.G.; Supervision, T.R. and A.G.; Project administration, D.H. and A.G.; Funding acquisition, A.G. All authors have read and agreed to the published version of the manuscript.

Funding: The research project STORT including the flight experiment was funded by the DLR's Program Directorate for Space Research and Development.

Data Availability Statement: The original contributions presented in this study are included in the article. Further inquiries can be directed to the corresponding author.

Conflicts of Interest: The authors declare no conflict of interest.

References

1. Anderson, J.D. *Hypersonic and High-Temperature Gas Dynamics*, 3rd ed.; American Institute of Aeronautics and Astronautics: Reston, VA, USA, 2019. [CrossRef]
2. Milos, F.S.; Chen, Y.-K. Ablation and Thermal Response Property Model Validation for Phenolic Impregnated Carbon Ablator. *J. Spacecr. Rockets* **2012**, *47*, 786–805. [CrossRef]
3. Zuber, C.; Reimer, T.; Esser, B.; Gülhan, A.; Herdrich, G.; Biller, N. Development of the Low-Density Phenolic-Based Fibrous Ablator ZURAM-K. *J. Spacecr. Rockets* **2021**, *58*, 415–424. [CrossRef]
4. Glass, D. Ceramic Matrix Composite (CMC) Thermal Protection Systems (TPS) and Hot Structures for Hypersonic Vehicles. In Proceedings of the 15th AIAA International Space Planes and Hypersonic Systems and Technologies Conference, Dayton, OH, USA, 28 April–1 May 2008; AIAA 2008-2682. [CrossRef]
5. Hald, H.; Weihs, H. Safety Aspects of CMC Materials and Hot Structures. In Proceedings of the Joint ESA-NASA Space-Flight Safety Conference, Noordwijk, The Netherlands, 11–14 June 2002; ESA SP-486.
6. Patel, M.; Saurabh, K.; Bhanu Prasad, V.V.; Subrahmanyam, J. High temperature C/C–SiC composite by liquid silicon infiltration: A literature review. *B. Mater. Sci.* **2012**, *35*, 63–73. [CrossRef]
7. Kochendörfer, R. Liquid silicon infiltration—A fast and low cost CMC-manufacturing process. In *Composites—Design, Manufacture and Application: Proceedings of the 8th International Conference on Composite Materials, Honolulu, HI, USA, 15–19 July 1991*; Woodhead Publishing: Cambridge, UK, 1991.
8. Reimer, T.; Petkov, I.; Koch, D.; Frieß, M.; Dellin, C. Fabrication and Characterization of C/C-SiC Material Made with Pitch-Based Carbon Fibers. In *Processing and Properties of Advanced Ceramics and Composites VII*; Mahmoud, M.M., Bhalla, A., Bansal, N.P., Singh, J.P., Castro, R.H.R., Manjooran, N.J., Pickrell, G., Johnson, S., Brennecka, G., Singh, G., et al., Eds.; The American Ceramic Society, John Wiley & Sons, Inc.: Hoboken, NJ, USA, 2015; pp. 277–296. [CrossRef]
9. Reichert, F.; Langhof, N.; Krenkel, W. Influence of Thermal Fiber Pretreatment on Microstructure and Mechanical Properties of C/C-SiC with Thermoplastic Polymer-Derived Matrices. *Adv. Eng. Mater.* **2015**, *17*, 1119–1126. [CrossRef]
10. Frieß, M.; Böyükbas, M.; Vogel, F.; Cepli, D.; Schatz, O.; Süß, F.; Shi, Y. Manufacture and thermomechanical characterization of wet filament wound C/C-SiC composites. *Int. J. Appl. Ceram. Tec.* **2022**, *19*, 34–44. [CrossRef]
11. Best, J.; Freudenberg, W.; Langhof, N.; Schafföner, S. Processing-microstructure correlations in material extrusion additive manufacturing of carbon fiber reinforced ceramic matrix composites. *Addit. Manuf.* **2024**, *79*, 103888. [CrossRef]
12. Shi, Y.; Li, S.; Sitnikova, E.; Cepli, D.; Koch, D. Experimental evaluation and theoretical prediction of elastic properties and failure of C/C-SiC composite. *Int. J. Appl. Ceram. Tec.* **2022**, *19*, 7–21. [CrossRef]
13. Buffenoir, F.; Zeppa, C.; Pichon, T.; Girard, F. Development and flight qualification of the C–SiC thermal protection systems for the IXV. *Acta Astronaut.* **2016**, *124*, 85–89. [CrossRef]
14. Böhrk, H.; Löhle, S.; Fuchs, U.; Elsäßer, H.; Weihs, H. FinEx—Fin Experiment on HIFiRE-5. In Proceedings of the 7th Symposium on Aerothermodynamics for Space Vehicles, Brugge, Belgium, 9–12 May 2011.
15. Böhrk, H.; Dittert, C.; Weihs, H.; Thiele, T.; Gülhan, A. Sharp Leading Edge at Hypersonic Flight: Modeling and Flight Measurement. *J. Spacecr. Rockets* **2014**, *51*, 1753–1760. [CrossRef]
16. Gülhan, A.; Hargarten, D.; Zurkaulen, M.; Klingenberg, F.; Siebe, F.; Willems, S.; Di Martino, G.; Reimer, T. Selected results of the hypersonic flight experiment STORT. *Acta Astronaut.* **2023**, *211*, 333–343. [CrossRef]
17. Di Martino, G.D.; Reimer, T.; Dauth, L.; Baier, L. Structure Design of a Sounding Rocket Fairing with a Segmented Filament Winding-Ceramic Matrix Composite Thermal Protection System. In Proceedings of the 2nd International Conference on High-Speed Vehicle Science Technology, Brugges, Belgium, 11–15 September 2022.
18. Reimer, T.; Di Martino, G.; Petkov, I.; Dauth, L.; Baier, L.; Gülhan, A. Design, Manufacturing and Assembly of the STORT Hypersonic Flight Experiment Thermal Protection System. In Proceedings of the 25th AIAA International Space Planes and Hypersonic Systems and Technologies Conference, Bengaluru, India, 28 May–31 June 2023; AIAA 2023-3089. [CrossRef]
19. Kochendorfer, R.; Lutzenburger, N.; Weihs, H. Joining Techniques for Fibre Ceramic Structures. *Adv. Compos. Lett.* **2004**, *13*, 75–85. [CrossRef]
20. Breede, F. Entwicklung Neuartiger Faserkeramischer C/C-SiC Verbundwerkstoffe auf Basis der Wickeltechnik für Raketendüsen. PhD Thesis, Universität Stuttgart, Stuttgart, Germany, 2017.
21. Böhrk, H.; Beyermann, U. Secure tightening of a CMC fastener for the heat shield of re-entry vehicles. *Compos. Struct.* **2010**, *92*, 107–112. [CrossRef]
22. Neuer, G.; Jaroma-Weiland, G. Spectral and Total Emissivity of High-Temperature Materials. *Int. J. Thermophys.* **1998**, *19*, 917–929. [CrossRef]
23. National Oceanic and Atmospheric Administration; National Aeronautics and Space Administration. *U.S. Standard Atmosphere, 1976*; Report Nr. NOAA-S/T-76-1562; U.S. Government Printing Office: Washington, DC, USA, 1976.

24. Hord, R.A. *An Approximate Solution for Axially Symmetric Flow over a Cone with an Attached Shock Wave*; Langley Aeronautical Laboratory, Langley Field, Va.; NACA Technical Note 3485; National Advisory Committee for Aeronautics: Washington, DC, USA, 1955.
25. White, F.M. *Viscous Fluid Flow*, 3rd ed.; McGraw-Hill: New York, NY, USA, 2006; pp. 15–44.
26. Van Driest, E.R. The Problem of Aerodynamic Heating. *Aeronaut. Eng. Rev.* **1956**, *15*, 26–41.
27. Mangler, W. *Grenzschichten an Rotationskörpern bei Symmetrischer Anblasung*; Bericht/A 17; Aerodynamische Versuchsanstalt: Göttingen, Germany, 1945; Volume 45.
28. Shi, Y.; Kessel, F.; Friess, M.; Jain, N.; Tushtev, K. Characterization and modeling of tensile properties of continuous fiber reinforced C/C-SiC composite at high temperatures. *J. Europ. Ceram. Soc.* **2021**, *41*, 3061–3071. [CrossRef]
29. RATH-Group. *Product Data Sheet ALTRA® 1500C*; RATH Group: Mönchengladbach, Germany, 2025.
30. Reimer, T. The EXPERT C/C-SiC Nose Cap—System Design and Thermomechanical Layout. In Proceedings of the AIAA/CIRA 13th International Space Planes and Hypersonics Systems and Technologies Conference, Capua, Italy, 16–20 May 2005; AIAA 2005-3262. [CrossRef]
31. *EN 1999-1-2*; Design of Aluminium Structures—Part 1–2: Structural Fire Design. Eurocode 9; CEN: Brussels, Belgium, 2007.
32. Jain, N.; Koch, D. Prediction of Failure in Ceramic Matrix Composites Using Damage-Based Failure Criterion. *J. Compos. Sci.* **2020**, *4*, 183. [CrossRef]
33. Reimer, T.; Di Martino, G.; Dauth, L.; Baier, L.; Gülhan, A.; Klingenberg, F.; Hargarten, D. STORT Hypersonic Flight Experiment Forebody Temperature Results. In Proceedings of the AIAA SCITECH 2025 Forum, Orlando, FL, USA, 6–10 January 2025; AIAA 2025-1342. [CrossRef]

Disclaimer/Publisher's Note: The statements, opinions and data contained in all publications are solely those of the individual author(s) and contributor(s) and not of MDPI and/or the editor(s). MDPI and/or the editor(s) disclaim responsibility for any injury to people or property resulting from any ideas, methods, instructions or products referred to in the content.